

SIMULATION OF 0-7.5 HZ DETERMINISTIC GROUND MOTIONS FOR MAXIMUM CREDIBLE EARTHQUAKE SCENARIOS AT THE LONG VALLEY DAM, CA

Kim Olsen and Te-Yang Yeh

Department of Geological Sciences
San Diego State University

Abstract

We have used 3D 0-7.5 Hz deterministic wave propagation to model the seismic response of the Long Valley Dam (LVD) in central California. The velocity structure, anelastic attenuation model, and the properties of the dam were calibrated via simulations of a $M_w 3.7$ event and the 1986 $M_w 6.3$ Chalfant Valley earthquake. Our nonlinear simulations of a $M_w 6.6$ Maximum Credible Earthquake scenario generate peak ground accelerations > 1 g at the LVD, where nonlinear damping (Drucker-Prager rheology) reduces PGAs predicted at the dam crest by a factor of 2.5. The simulations predict relative displacements of the dam material of ~ 10 cm.

Introduction

Failure of dams during seismic shaking can have devastating societal consequences. While well-designed Earth dams have generally performed well during earthquake ground shaking (FEMA, 2005), catastrophic failures have still occurred due to various reasons, depending on the ground shaking level, structure design, and material properties (FEMA, 2005; Seed et al., 1978). In this work, we have carried out 3D numerical simulations to predict the seismic response of the Long Valley Dam (LVD) for a Maximum Credible Earthquake (MCE). The LVD is a 55 meter high embankment dam located 35 km northwest of Bishop, CA, just east of the Sierra Nevada range. The completion of the dam in 1941 created Lake Crowley which has been serving as a storage unit for the Los Angeles aqueduct as well as a flood control unit. The major part of the dam consists of extensive rolled earth-fill core (Lai and Seed, 1985). The dam has an array of accelerometers located on the dam crest, downstream wall, abutment and downstream bedrock (Fig. 1, left).

The seismic response of the LVD has been extensively studied in which the soil behavior was modeled by different approaches. Lai and Seed (1985) accounted for the nonlinear response of the dam material by using equivalent linear soil properties. Later studies used more rigorous numerical methods (e.g., finite-elements) to simulate the nonlinear hysteretic behavior of the dam material under cyclic loading with multi-surface plasticity theory (Griffiths and Prevost, 1988; Yiagos and Prevost, 1991; Zeghal and Abdel-Ghaffar, 1992). A potential limitation of the earlier studies is the treatment of the excitation of the dam to estimate the seismic response. Typically, stability analyses for dams use an accelerogram of a historical event, for example, recorded near the downstream base as input motion. Conventionally, the same input ground motion is applied at input nodes along the bottom and sides of the dam, approximating the excitation resulting from a vertically incident plane wave. Such assumption may represent an

oversimplification, as it does not account for scattering caused by heterogeneities at all scales. In addition, modeling the dam response using existing records usually requires scaling of the amplitudes, which is now generally a discouraged practice.

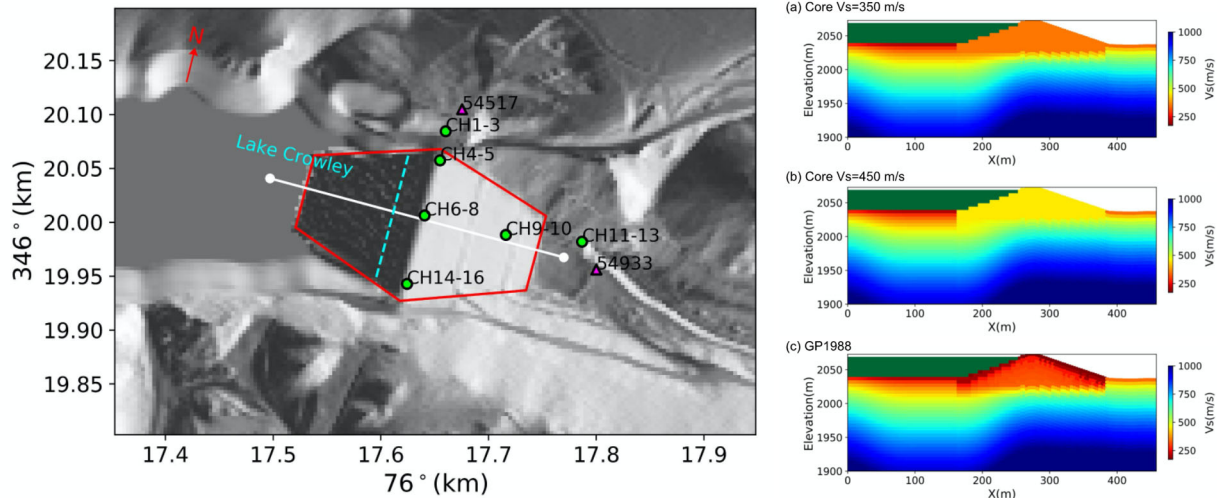


Figure 1: (left) Map view of the Long Valley dam. Blue dashed line depicts the contact of the lake water surface on the upstream face. Green-filled circles are sensor locations in the structure array (station code 54214) installed on the LVD. Magenta triangles are nearby stations, which were used for estimating the geotechnical layer (GTL) tapering depth. (right) 2D V_s transects across the LVD extracted from the three different dam models tested in this study. The dam core in models (a) and (b) is homogeneous, whereas that in (c) has a layered structure computed from the elastic parameters used in Griffiths and Prevost (1988).

The Hilton Creek Fault (HCF) is a significant range-bounding normal fault at the eastern side of the Sierra Nevada Mts. Because it passes just 8 km west of the LVD, it has been identified as a possible source for the MCE that could potentially damage the LVD (Lai and Seed, 1985). Scenario earthquakes on the HCF were also considered in a recent study on earthquake hazards for the Long Valley Caldera-Mono Lake Area by Chen et al. (2014). However, the methods used in this study were based primarily on ground motion prediction equations (GMPEs) which provided only peak ground motion amplitudes and spectral accelerations with very limited spatial resolution. In addition, GMPE-based approaches provide only rudimentary control on the effects of the source parameters, with no support of the complete time history of particle motions (FEMA, 2005). In this study, we utilize the power of supercomputers to address these issues by performing fully-coupled 3D deterministic simulations considering both linear and nonlinear response of the material within the LVD and its surroundings. Our simulation approach enables us to fully account for source, path, and site effects in a single numerical model.

Numerical method

We use the 4th-order accurate finite-difference code AWP-ODC, with support for frequency-dependent attenuation (Cui et al., 2010; Withers et al., 2015). In order to reduce the computational cost, we used 3 velocity meshes separated vertically with a factor-of-three

increase in grid spacing with depth (3.5 m, 10.5 m, and 31.5 m) via a discontinuous mesh approach (Nie et al., 2017). We used a minimum shear wave velocity of 175 m/s in the top block, ensuring at least 6.7 points per minimum wavelength (O'Reilly et al., 2021).

Support for surface topography is needed to model the seismic response of the LVD. For the validation work of the 2015 M_w 3.7 event, we used the curvilinear grid approach by O'Reilly et al. (2022). However, this version of AWP-ODC does not yet support nonlinear soil response calculations. For this reason, we performed the validation with the 1986 M_w 6.2 Chalfant Valley event and simulations of the HCF scenarios using a Cartesian-grid version of AWP-ODC with a vacuum formulation for the free surface (Graves, 1996). Previous studies clearly show that the accuracy of the vacuum formulation is reduced, as compared to explicit free surface formulations. However, we verified the seismic response of the LVD using the vacuum formulation, as compared to those from the curvilinear solution, to ensure that our analysis of the LVD is sufficiently accurate (not shown).

Velocity model

Our reference model is extracted from the SCEC CVM version 4.26-M01 (CVM-S in the following, Small et al., 2017). It has been shown (Ely et al., 2010; Hu et al., 2022) that CVM-S generally causes underprediction of peak amplitudes and coda duration outside the basins, due to unrealistically high near-surface velocities. To alleviate this underprediction, Ely et al. (2010) proposed a simple generic overlay-based tapering of time-averaged shear wave velocity (V_s) in the top 30 m (V_{s30}) to merge with tomography at a depth of 350 m. Hu et al. (2022) found that applying the taper to deeper depths (700-1,000 m) significantly improved the fit between deterministic synthetics and strong motion data for the 2014 M_w 5.1 La Habra earthquake in the greater Los Angeles area. Following this approach, we estimate the optimal tapering depth for the near-surface material near the LVD in the Sierra Nevada Mts.

For the surface topography, we used the 1m-resolution digital elevation model (DEM) from the U.S. Geological Survey. This DEM does not provide elevations of areas under water, including part of the upstream face and the entire Lake Crowley. As we need to include the lake water directly into our simulations, we made the following adjustments to the DEM. First, we removed the lake water from the DEM by manually lowering the elevations of the grids located inside the lake from 2066 m to 2036 m, assuming a flat lake bed and an average water depth of 30 m. Secondly, we mirrored the surface elevations of the downstream face to the upstream side with respect to the center line of the crest of the dam (axis of the dam), assuming symmetry of the LVD with respect to the axis of the dam. We then applied Gaussian filters of 7 m resolution to smooth the topography around the edges of the area where we removed the lake water, to minimize artifacts introduced by these adjustments. In our calculations, the lake water is modeled as a purely elastic material with $V_p=1,050$ m/s, $V_s=0$ m/s, and $\rho=1,492$ kg/m³, and the bathymetry of areas under lake water, including the lower portion of the upstream face, are described in a staircase fashion.

Anelastic attenuation

In our simulations, we adopted a frequency-dependent attenuation model where Q_s values are given by

$$Q_s(f) = Q_{s,0}, \quad f < f_0,$$

$$Q_s(f) = Q_{s,0} \left(\frac{f}{f_0} \right)^\gamma, \quad f \geq f_0,$$

where the power-law exponent γ controls the rate of increase of Q_s above the transition frequency, f_0 , set at 1 Hz (Withers et al., 2015), and $Q_{s,0}$ is a constant Q_s value. Following Olsen et al. (2003), we assumed $Q_{s,0}$ to be proportional to the local S-wave speed, $Q_{s,0} = kV_s$, where k is a parameter specific to the study area. For simplicity, the relationship of $Q_p = 2Q_s$ was assumed throughout this study, following the findings of Olsen et al. (2003). The parameters k and γ are estimated in Section **Anelastic Attenuation**.

Validation I: 2015 M3.7 event

Our first validation event is a M_w 3.7 earthquake from 2015. Due to its small magnitude, it is reasonable to approximate this event as a point source, thereby eliminating uncertainty of modeling finite-fault effects. For this reason, we use this event to constrain the anelastic attenuation parameters for the layers in our model domain as well as the depth of the GTL. This event has a normal-faulting focal mechanism ($158^\circ/75^\circ/-103^\circ$, $20^\circ/20^\circ/-50^\circ$) and is located 7 km to the west of the LVD (-118.7878° , 37.5975°) at a depth of 4.8 km (Fig. 2, left). In this analysis we focused on the ground accelerations recorded by strong motion sensors installed on and nearby the dam (structure array 54214, stations 54517 and 54933) which are operated under California Strong Motion Instrumentation Program (CSMIP) with network code CE.

Source description

To describe the source of the M_w 3.7 event, we assume a Brune-type spectral shape (Brune, 1970) with a f^{-2} decay at frequencies above the corner frequency (f_c), given by

$$M(f) = \frac{M_0}{1 + (f/f_c)^2},$$

where M_0 is the seismic moment. After an inverse Fourier transform of the source spectrum with the constraint of minimum phase, the moment rate function has the following expression in the time domain,

$$M(t) = \frac{t}{T_c^2} e^{-\frac{t}{T_c}},$$

where T_c is the characteristic time controlling the width of the pulse, which depends on the corner frequency $T_c = 1/2\pi f_c$. We determined the corner frequency using

$$f_c = k\beta \left(\frac{16 \Delta\sigma}{7 M_0} \right)^{\frac{1}{3}},$$

where k is a constant, β is the V_s at the source (3,410 m/s), and $\Delta\sigma$ is the stress drop. Using $k = 0.32$ assuming a circular rupture with a rupture speed of $V_r = 0.9V_s$ and a stress drop of 3 MPa, we get $T_c = 0.0593$ s, and $f_c = 2.7$ Hz.

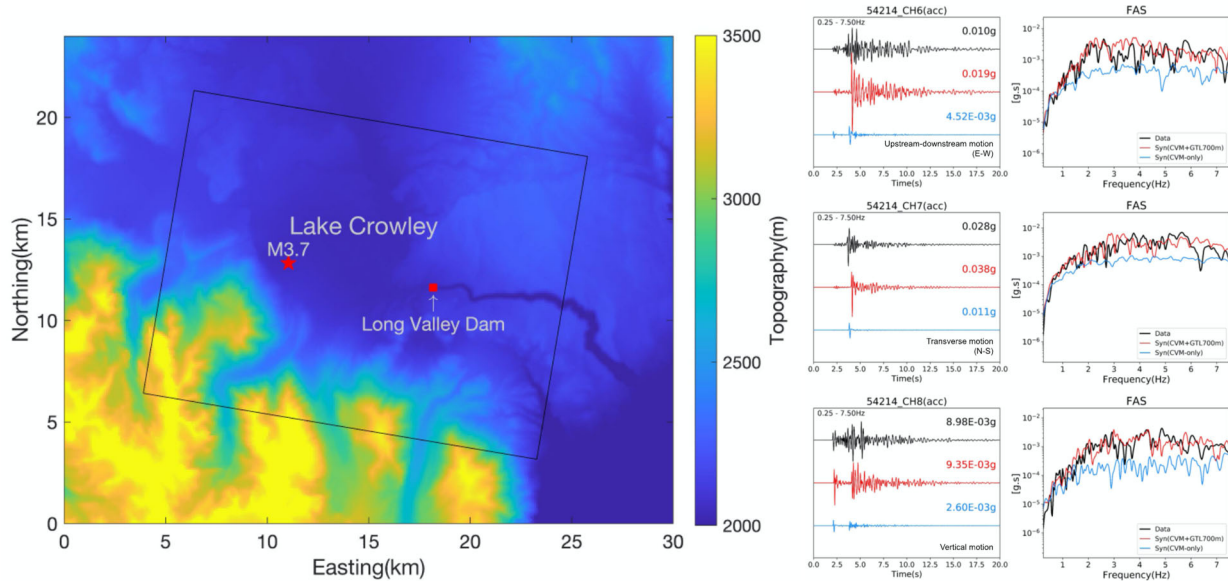


Figure 2. (left) Model domain (black rectangle) for the simulations of the 2015 $M_w 3.7$ earthquake (rotated 9.51° clockwise, model depth 15 km). (right) Comparison of data (black traces) and synthetics (red and blue traces) in the time and FAS domains at sensors located at the dam crest (see Fig. 1 for sensor location). The red synthetic traces were computed with CVM-S, a GTL tapered to 700 m below the free surface, and a dam core with 450 m/s, whereas the blue traces were computed with CVM-S only (no GTL).

Near-surface geotechnical layer (GTL)

We follow the approach of Hu et al. (2022) to calibrate the near-surface velocity structure within our model domain. This calibration entails replacing the velocity model extracted from the SCEC CVM-S, from the free surface to a given tapering depth (z_T) with V_P , V_S , and ρ computed using the formulations of Ely et al. (2010) along with local V_{S30} information. This approach provides a smooth transition between the near-surface velocity structures and the original model. We used the measured V_{S30} values wherever available, and the values from Wills et al. (2015) elsewhere.

In order to estimate an optimal value for the tapering depth z_T , we compared simulations for models with GTL implemented with z_T of 350 m, 700 m, and 1,000 m to seismic data recorded off the dam (e.g., stations 54517 and 54933). Based on this analysis, we used z_T equal to 700 m in our simulations. This modification resulted in significantly lower V_S values near the surface of the domain as well as a higher degree of spatial complexities compared to CVM-S.

Elastic properties of the LVD

Earlier studies have modeled the LVD with an extensive rolled earthfill clay core, which constitutes the major portion of the dam structure with a thin layer of more permeable rock-fill shell on top (Lai and Seed, 1985; Yiagos and Prevost, 1991; Griffiths and Prevost, 1988). We explored different V_S for the homogeneous dam core as well as more complicated descriptions (see Fig. 1, right), using the $M_w3.7$ event. Our tests show that a homogeneous core with $V_P=1,000$ m/s, $V_S=350$ m/s, and $\rho=2,110$ kg/m³ (Fig. 1, right, top) as well the presence of a thin shell with low V_S values used in the Griffiths and Prevost (1988)'s modeling (Fig. 1, right, bottom) overpredict the observed acceleration amplitudes (not shown here). On the other hand, our simulations show that using a homogeneous core with $V_P=1,000$ m/s, $V_S=450$ m/s, and $\rho=2,110$ kg/m³ (Fig. 1, right, center) provides an unbiased prediction of the observed ground motions in both time and frequency domains. Due to its homogeneous nature, this model makes no distinction between the core and shell of the dam. We note that this model is fairly close to the actual structure of LVD, as an extensive rolled earthfill clay core constitutes the major portion of the dam structure with a thin layer of a more permeable rock-fill shell on top (Lai and Seed, 1985; Yiagos and Prevost, 1991; Griffiths and Prevost, 1988).

Anelastic attenuation

We carried out a grid search to estimate the values of k and γ that provide the best fit to the strong motion records for the $M_w3.7$ event at the LVD. These simulations included the estimated optimal GTL parameters and elastic properties of the dam, with recorded data both on and near the LVD. As an estimate of goodness-of-fit (GOF) we used the natural logarithm of the observed-to-simulated acceleration Fourier amplitude spectral ratio for all available channels, given by

$$GOF_{FAS}(f) = \ln \left(\frac{FAS_{obs}(f)}{FAS_{model}(f)} \right),$$

where $FAS_{obs}(f)$ and $FAS_{model}(f)$ are Fourier amplitude spectra of observed and simulated acceleration waveforms, respectively. Prior to computing the spectral ratio, both $FAS_{obs}(f)$ and $FAS_{model}(f)$ were smoothed with a Savitzky-Golay filter (Savitzky and Golay, 1964) with a 0.5 Hz window length to suppress large fluctuations. We calculated the mean GOF_{FAS} and the corresponding standard deviation between 0.2-7.5 Hz to quantify the model performance. Due to the definition of GOF_{FAS} , a positive value indicates under-prediction and vice versa. In addition, we defined an error value as a summary of the mean GOF_{FAS} over the entire frequency range,

$$Error = \frac{\sum_{i=1}^{Nf} |\mu_i|}{Nf},$$

where μ_i is the mean GOF_{FAS} at frequency point i . The GOF_{FAS} analysis shows a trade-off between k and γ , where $(k = 0.05, \gamma = 0.4)$, $(k = 0.075, \gamma = 0.2)$, and $(k = 0.1, \gamma = 0)$ result in almost identical GOF_{FAS} curves. Based on this result, we proceeded with an intermediate model with $k = 0.075$ and $\gamma = 0.2$ in all following simulations.

Validation results

Our numerical simulation was able to generate synthetics that are reasonably close to the data in both time and frequency domains (see Fig. 2, right). The FAS of the full model (red trace in Fig. 2, right) shows no systematic bias where the model without a geotechnical layer clearly underpredicts the spectral energy across almost the entire frequency range. In summary, the attenuation model using $k = 0.075$ and $\gamma = 0.2$, the homogeneous dam structure with $V_P=1,000$ m/s, $V_S=450$ m/s, $\rho=2,110$ kg/m³, along with a geotechnical layer in the top 700 m are capable of providing unbiased estimates of the recorded ground motions in both time and frequency domains up to 7.5 Hz.

Validation II: The 1986 $M_w6.2$ Chalfant Valley earthquake

We used the 2015 $M_w3.7$ event (Validation I, point source) to validate the CVM-S velocity model for the area, calibrate the attenuation model, and confirm the implementation of the GTL and the 3D structure of the LVD. The model was then used for the second validation event, namely the 1986 $M_w6.2$ Chalfant Valley earthquake. This earthquake is located 25 km to the east of LVD, which requires a larger computational domain to accommodate the entire fault and LVD (Fig. 3, left). The moment magnitude of this event ($M_w6.2$) clearly warrants a finite-fault description for its rupture. We use the Graves and Pitarka (2016) kinematic rupture generator to generate finite-fault descriptions for the Chalfant Valley event, described in the following section.

Finite-fault source model

The hypocenter locations for the Chalfant Valley earthquake reported by previous studies are fairly similar (varying horizontally ≤ 1 km), while the interpretation of the focal mechanism and the fault dimensions show larger variation (Smith and Priestley, 2000; Cockerham and Corbett, 1987; Pacheco and Nábelek, 1988; Savage and Gross, 1995). Based on the published focal mechanisms for the event (Cockerham and Corbett, 1987; Pacheco and Nábelek, 1988; Savage and Gross, 1995; Smith and Priestley, 2000), we assume a pure strike-slip focal mechanism in our simulations.

Following the hypocenter location and the interpreted fault length in Smith and Priestley (2000, 13.9 km), we used a fault width of 11.6 km from the empirical source scaling relations by Leonard (2014) for a $M_w6.2$ event (moment $2.65 \cdot 10^{18}$ Nm), with strike/dip/rake of $150^\circ/55^\circ/-180^\circ$ and hypocenter location of $(-118.4408^\circ, 37.5333^\circ, 10.8$ km). Using the Graves and Pitarka

(2016) kinematic rupture generator, we generated three realizations of slip distributions for the defined fault plane, focal mechanism and hypocenter.

Validation results

We generated synthetic seismograms for the Chalfant Valley event, including a GTL tapered to a depth of 700 m below the free surface and a homogeneous dam core with $V_S=450$ m/s. We found that the three source realizations for the Chalfant Valley event result in similar GOF_{FAS} values, where the model predictions are generally unbiased across the entire examined frequency range. As shown in Fig. 3, right (only showing seed #2), the synthetics are in reasonable agreement with the data recorded at different locations on the LVD in both time and frequency domains up to 7.5 Hz. We note that the Chalfant Valley earthquake validation was carried out using purely elastic rheology, as the PGAs at the dam (about 0.1 g) were deemed insufficient to trigger significant nonlinear soil behavior.

Hilton Creek Fault scenarios

As shown above, our validations for the $M_w3.7$ and the $M_w6.2$ 1986 Chalfant Valley earthquakes resulted in well-calibrated velocity and attenuation models for the area. In addition, the results of the modeling of the Chalfant Valley event demonstrate that the Graves and Pitarka (2016) kinematic rupture generator is able to create source descriptions that produce ground motions in agreement with data for frequencies up to 7.5 Hz using deterministic simulations. We are therefore ready to perform simulations for scenario earthquakes to assess the stability of the LVD. The Hilton Creek Fault (HCF) is a significant range-bounding normal fault at the eastern side of the Sierra Nevada. Because of its closest distance to the LVD of just 8 km, it has been identified as a possible source for the MCE that could significantly affect the stability of the dam (Lai and Seed, 1985; Chen et al., 2014). Figure 4 (left) shows the model domain for the HCF scenarios, and Table 1 lists the modeling parameters.

Source description

We designed scenarios with $M_w6.6$ on the HCF with a fault length of 21 km and a width of 13.3 km estimated using the empirical magnitude-area relations by Leonard (2010). The $M_w6.6$ scenario is one of three cases presented in a study by Chen et al. (2014) for assessing the seismic hazard of the Long Valley Caldera area associated with the HCF. In addition to the $M_w6.6$ scenario, the study also considered $M_w6.5$ and $M_w6.8$ scenarios. However, Chen et al. (2014) pointed out that the fault rupture for the $M_w6.8$ scenario needs to extend into the Long Valley Caldera with a geometry that violates both geologic and kinematic constraints (Hill and Montgomery-Brown, 2015). Assuming that the hazards to the LVD from the $M_w6.5$ are smaller, we chose the $M_w6.6$ scenario to represent the MCE. Based on the estimate of Chen et al. (2014), the recurrence interval for this scenario is 204 years.

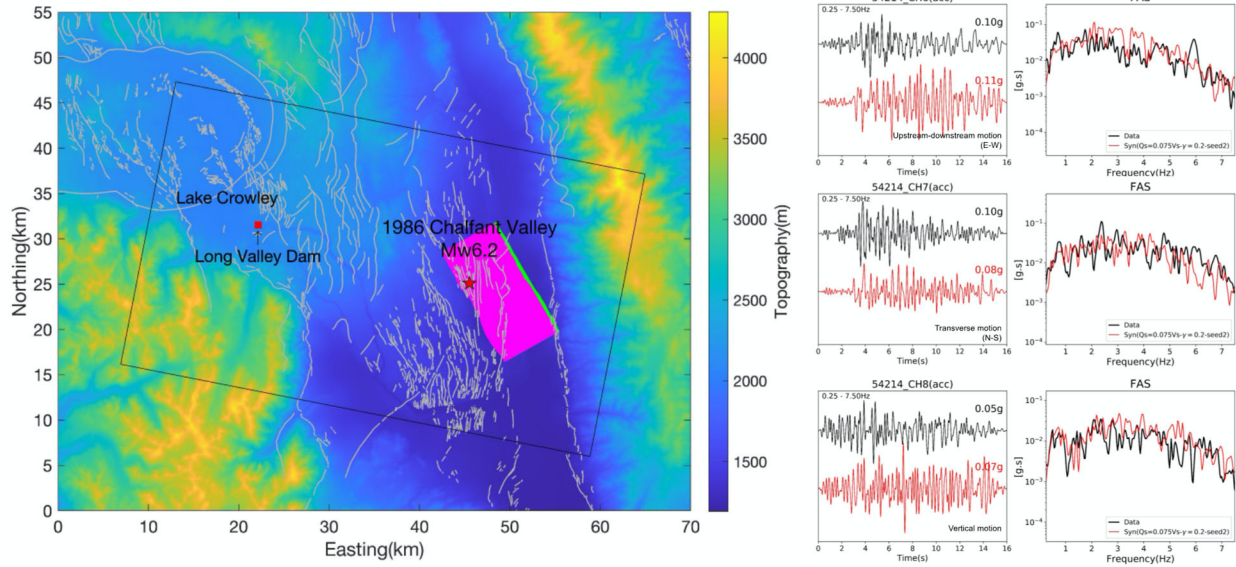


Figure 3: (left) Location map for the simulation domain of the 1986 $M_w6.2$ Chalfant Valley earthquake (rotated 11.08° clockwise, model depth 30.75 km). The black box depicts the simulation domain for the earthquake. The pink area shows the surface projection of our finite fault source for the event, the red star shows the epicenter location and the green line depicts the top edge of the fault plane at 2.5 km depth. Green triangles depict station locations. (right) Comparison of data (black traces) and synthetics (red traces) in the time and the FAS domains at sensors located near the downstream base. The synthetic traces were computed with CVM-S, a GTL tapered to 700 m below free surface, and a dam core with $V_s=450$ m/s (see Fig. 1 for sensor location).

Three different rupture scenarios with the same slip distribution were selected to capture the range of ground motions generated among a southward, northward and a bilateral rupture mode (Fig. 4, right). The hypocenters of all three rupture scenarios are located 6 km down-dip from the top of the fault, all featuring surface ruptures. The source parameters of the HCF scenarios are listed in Table 2.

Elastic and nonlinear properties of materials

For the HCF simulations we used the SCEC CVM-S with a GTL layer tapered to 700 m, $Q_s = 0.075V_s f^{0.2}$, and $Q_p = 2Q_s$, the preferred model for the $M_w3.7$ and Chalfant Valley earthquake validations. In the HCF scenarios, we included nonlinear response of the material in our simulations using the Drucker-Prager yield condition (Drucker and Prager, 1952), where the material behaves purely linear until the yield stress is reached. The implementation of Drucker-Prager plasticity in AWP-ODC is based on the work of Roten et al. (2016). The non-associated Drucker-Prager plasticity is regularized using time-dependent relaxation (Andrews, 2005) via the return map algorithm, following the guidelines of the SCEC/USGS (U.S. Geological Survey) dynamic earthquake rupture code verification exercise (Harris et al., 2011). The Drucker-Prager yield stress $Y(\sigma)$ is defined as

$$Y(\sigma) = \max(0, c \cos\phi - (\sigma_m + P_f) \sin\phi)$$

where c is the cohesion, ϕ is the friction angle, P_f is the fluid pressure, and σ_m is the mean (normal) stress ($\sigma_{xx} + \sigma_{yy} + \sigma_{zz}$). The yield stress includes the hydrostatic condition for the fluid pressure, linearly increasing with depth below the water level. The water level inside the dam follows the pre-defined phreatic line shown in Fig. 5. We set $P_f = 0$ for all material above the phreatic line inside the dam.

Table 1: Simulation parameters for the Hilton Creek fault $M_w 6.6$ MCE scenarios

Domain	
Length	28.72 km
Width	40.82 km
Depth	30.68 km
Southwest corner	$-118.84019^\circ, 37.37252^\circ$
Northwest corner	$-118.96107^\circ, 37.72752^\circ$
Southeast corner	$-118.52681^\circ, 37.43966^\circ$
Northeast corner	$-118.64633^\circ, 37.79500^\circ$
Rotation angle	14.01° counterclockwise from north
Spatial resolution	
Maximum frequency	7.5 Hz
Minimum V_S	175 m/s
Points per minimum wavelength	6.66
Grid spacing	3.5 m 4.23 km above sea level to 0.24 km below sea level
	10.5 m 0.22 km to 2.56 km below sea level
	31.5 m 2.49 km to 30.68 km below sea level
Temporal resolution	
Time step	0.00027 s
Simulation time	40 s

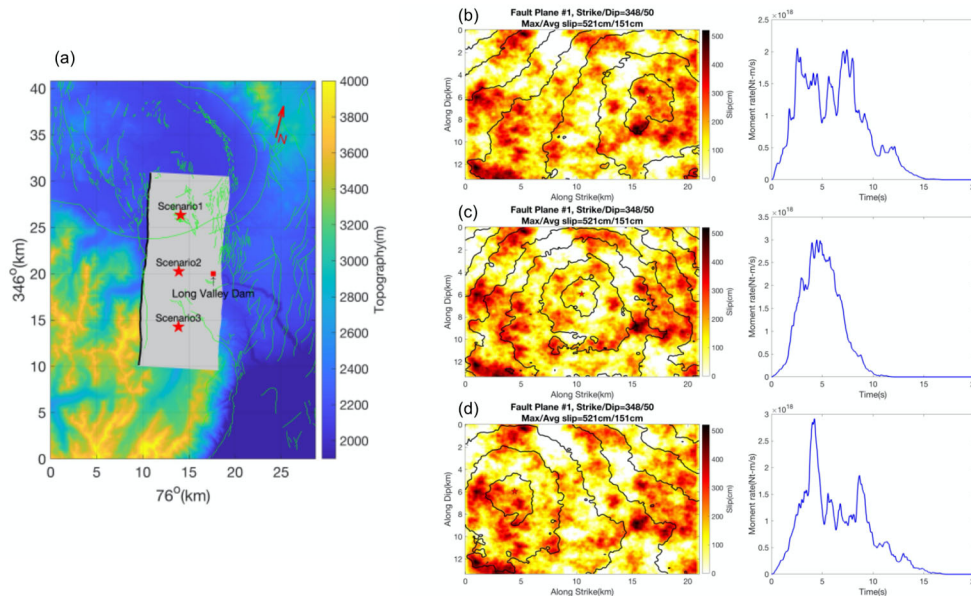


Figure 4: (left) Surface projection of the fault plane for the HCF scenarios, with epicentral locations for the 3 rupture scenarios (stars). (right) Slip (colors) and rupture time contours as well as moment rate histories (on the right of each slip model) for the 3 HCF scenarios with (a) southward, (b) bilateral and (c) northward rupture modes. Red stars on the slip models depict the rupture initiation locations.

Table 2: Source parameters for the Hilton Creek fault M_w 6.6 MCE scenarios

Hypocenter location	Southward rupture: $Lon. : -118.7638^\circ$ $Lat. : 37.6347^\circ$ $Depth : 4.8$ km Bilateral rupture: $Lon. : -118.7481^\circ$ $Lat. : 37.5813^\circ$ $Depth : 4.6$ km Northward rupture: $Lon. : -118.4408^\circ$ $Lat. : 37.5291^\circ$ $Depth : 4.3$ km
Focal mechanism ^a	strike/dip/rake= $348^\circ/50^\circ/-90^\circ$
Fault dimensions ^b	Length=21 km Width=13.3 km

^a: U.S. Geological Survey Quaternary fault and fold database (Haller *et al.*, 2004)

^b: Leonard (2010)

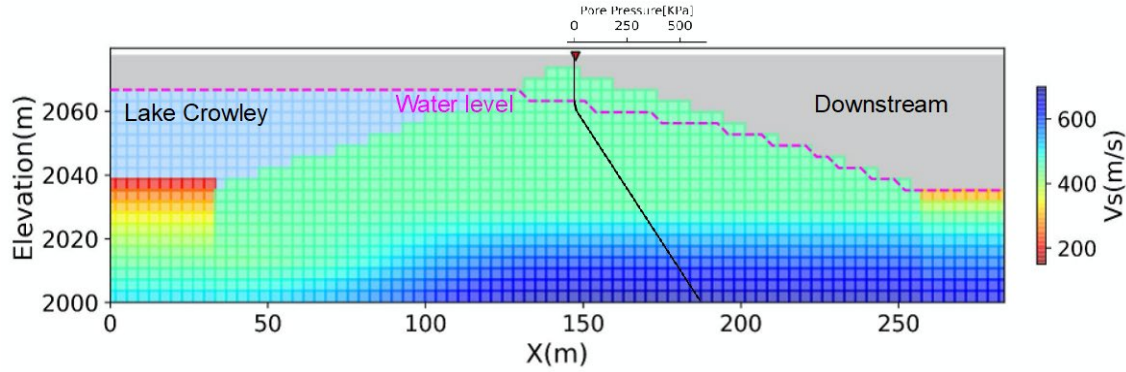


Figure 5. Water level assumed for the nonlinear simulations. The black line shows pore pressure as a function of depth.

For the material within the dam, we assumed a cohesion of 45 kPa and a friction angle $\phi=39^\circ$, as was used for the core material as described in Griffiths and Prevost (1988). To determine the yield stress of material off the dam, we adopted the generalized Hoek-Brown failure criterion that conveniently provides the effective cohesion and a friction angle needed for the Drucker-Prager yield condition (Hoek *et al.*, 2002). The Hoek-Brown failure criterion uses a Geological Strength Index (GSI) value for each material. As the mechanical properties of near-surface material are poorly constrained, we make the assumption that GSI is correlated with the local shear wave speed (V_s). The V_s and GSI measurements for rock samples in southern California by Townsend *et al.* (2021) (Figure 5 of their study) illustrate the relationship between these two quantities. Their analysis shows that (1) rocks with V_s of 200-300 m/s can be characterized by a GSI of 20, (2) GSI of rock samples with V_s of 300-500 m/s fall in the 20-40 range, and (3) rocks with V_s of 1,500 m/s are usually associated with GSI values of ~ 90 . Based on these observations, we first assigned each material into a category based on its S-wave speed, and used the corresponding relationship to compute the GSI value:

$$GSI = \begin{cases} 20 & \text{if } V_s < 300m/s \\ 20 + (V_s - 300) \times \frac{40-20}{500-300} & \text{if } 300m/s \leq V_s < 500m/s \\ 40 + (V_s - 500) \times \frac{90-40}{1500-500} & \text{if } 500m/s \leq V_s < 1500m/s \\ 90 + (V_s - 1500) \times \frac{100-90}{2000-1500} & \text{if } 1500m/s \leq V_s < 2000m/s \\ 100 & \text{if } V_s \geq 2000m/s \end{cases}$$

HCF Scenario Ground Motion Results

We performed both linear and nonlinear simulations for the proposed HCF scenarios, in order to quantify the latter effects. Our results show that the variation of hypocenter location can cause variation of PGA predicted at the crest top by a factor of 1.5. Moreover, the predicted ground accelerations are lower around the downstream base as compared to the dam crest, which demonstrates that the structure of the dam itself amplifies the ground motion by a factor of 2 or more. Given that the southward rupture scenario produces the largest ground motions overall, we focus on this scenario in the following analysis. Fig. 6 illustrates the differences between the linear and nonlinear behavior at the crest center and downstream sensor locations. Notice the strong reduction of the PGAs due to nonlinear response of the material, up to a factor of 2.5, where we predict stronger reductions on the dam as compared to off the dam. These results indicate that nonlinear effects are significant for the ground motions at the LVD.

We illustrate the ground motion response of the dam for the HCF scenarios along a 2D transect across the dam (white line crossing the dam in Fig. 1). Fig. 7 shows that both peak ground velocities (PGVs) and PGAs are amplified along the surface of the dam. The largest PGVs occur at the center crest while the largest PGAs are found in the middle of the downstream face, in particular in the region between the downstream face and the phreatic line. This is expected as the material above the phreatic line is exposed to less nonlinear damping due to lack of fluid pressure, and therefore stronger ground motions. Also notice the 50 m by 20 m zone of elevated PGAs at the base of the dam, right beneath the crest, likely originating from interaction between the dam and the underlying material.

We followed the approach in Ma (2008) to calculate the accumulated strain values, η (Fig. 8). As mentioned in Ma (2008), this quantity is a good representation of actual material damage since it is the cumulative norm of the strain-tensor increments throughout the simulation and thus does not decay through time. The largest cumulative strain occurs in the upstream part of the dam, and areas of the downstream side, near the surface of the upstream and downstream faces, with values up to about 1%. Since the calculation includes all of the dynamic strain, the values in Fig. 8 are expected to be larger than the strain computed from the final permanent displacement field.

Settlement of the dam after a seismic event is crucial information for evaluating dam stability. We computed the relative displacements inside the dam along the 2D transect (Fig. 1) with respect to a control point below the lake as a proxy of the settlements (Fig. 9). Our simulation predicts primarily east-southeastward movement of the material on the upstream face by approximately 10 cm with 3 cm south-southwestward movement near the crest, and very little uplift of displacements with respect to the control point ($< |2|$ cm). The spatial extent of the relative horizontal movement of the LVD is confined to the upper half of the dam. The maximum displacements are about 0.2% of the height of the LVD.

To further assess the response of the LVD during the MCE scenario, we extracted synthetic waveforms every 7 m along a vertical array from the top to the base of the dam (see Fig. 10). As can be seen in the horizontal motions (Figs. 11-12), the high-frequency signal present in both acceleration and velocity waveforms at the bottom of the dam (elevations 2017 m

and 2024 m) gradually vanishes toward the crest top, where the amplitude first decreases between 2017 m and 2045 m, and then increases by nearly a factor of 2 from 2045 m to 2073 m (crest). Figs. 11-13 show acceleration and velocity waveforms, comparison of linear and nonlinear waveforms at the surface, and FAS at three select locations along the array. The FAS show that the elevated energy between 4-6 Hz in the waveforms at 2017 m is absent in the record at 2045 m, while the energy between 2-4 Hz is enhanced in the 2045 m record. The migration of energy from high to low frequency is a result of nonlinear soil behavior. Approaching the crest top, the seismic waves are further amplified by the shape of the dam structure at frequencies above 2 Hz. On the other hand, the vertical ground motions show increased amplitudes approaching the crest top without the high frequency energy depletion found on the horizontal components (Fig. 13). The reason for this is likely that the vertical component primarily contains P-waves which are less likely to trigger nonlinearity. Our results show that the combined effects of nonlinearity and the structure of the dam result in complex ground motion patterns inside the LVD.

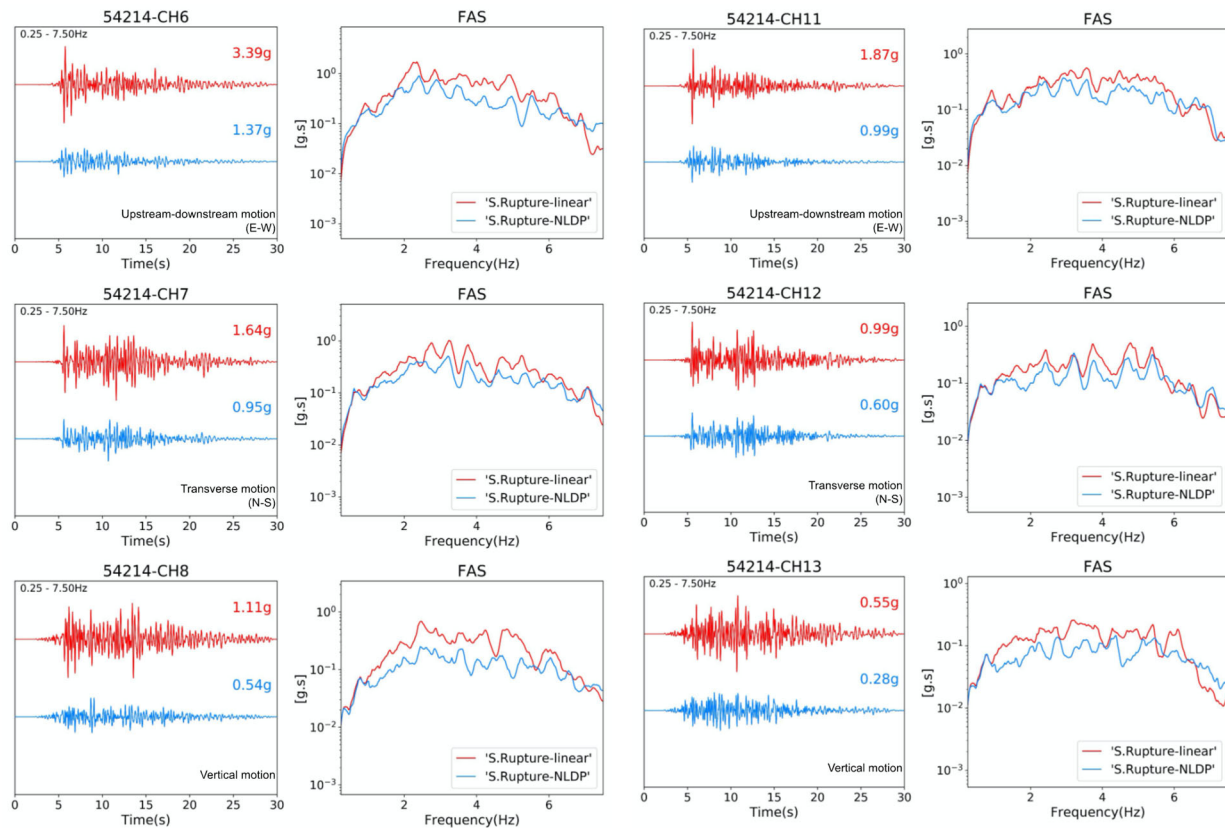


Figure 6: Comparison of linear (red traces) and nonlinear (blue traces) synthetics computed for the southward rupture scenario in the time and FAS domains at sensors located at the (left) crest center and the (right) downstream base (see Fig. 1 for sensor location).

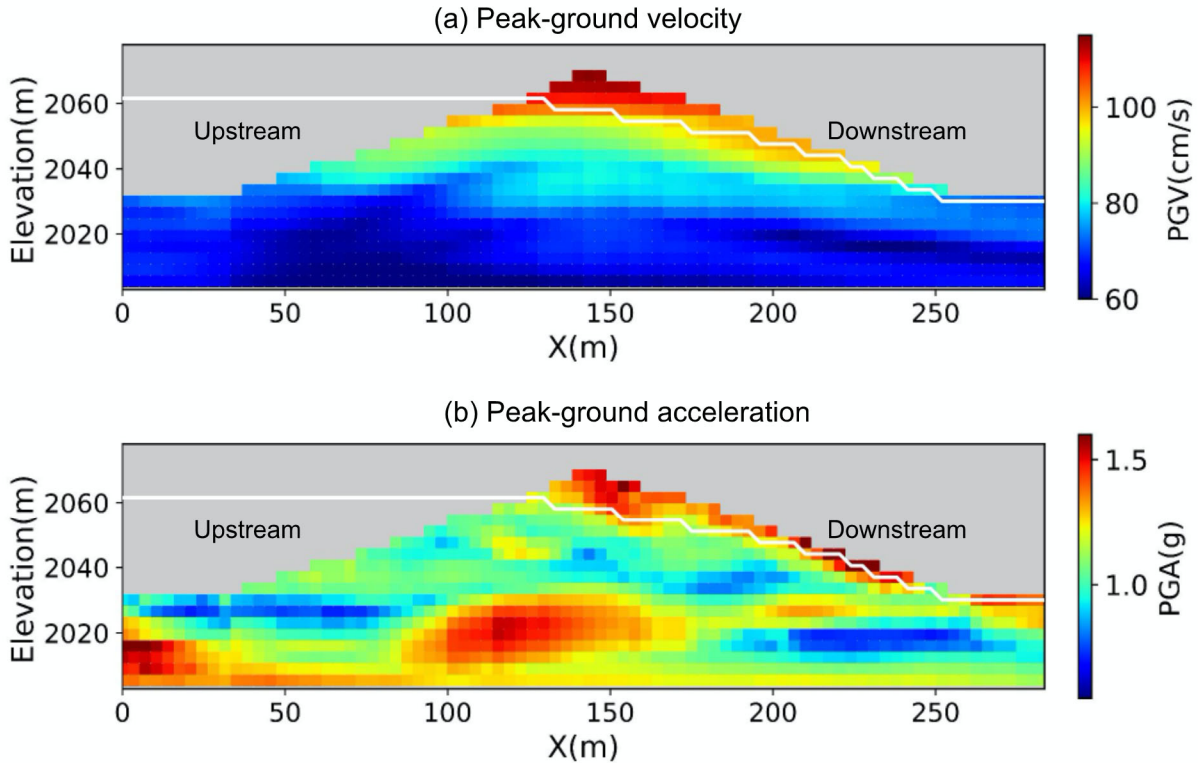


Figure 7. (top) PGV and (bottom) PGA from HCF southward rupture scenario along the transect shown by the white line in Fig. 1.

Discussion and conclusions

The goal of this study is to predict broadband (0-7.5 Hz) ground motions at the LVD for MCE scenarios that are expected to significantly affect the stability of the dam. To ensure that our predicted ground motions are accurate, we first conducted two validations, namely using (1) a 2015 $M_w 3.7$ event with a point source representation and (2) the 1986 $M_w 6.2$ Chalfant Valley earthquake modeled by finite-fault sources. During the first validation we calibrated the tapering depth for the near-surface GTL representation to $z_T = 700$ m, with relatively small differences for z_T between 350-1000 m. Furthermore, we estimated optimal parameters $k=0.075$ and $\gamma=0.2$ for the relation $Q_s(f) = kV_s f^\gamma$ (V_s in m/s), as well as for the velocity structure of the dam. Using these calibrated models, we showed that our numerical simulation results can generate 0-7.5 Hz wavefields that are in good agreement with data. Finally, we successfully extended the validation to finite-fault sources for the 1986 Chalfant Valley event using the Graves and Pitarka (2016) kinematic rupture generator.

Very limited direct measurement of the material properties of the LVD is available. A numerical study on the seismic response of the LVD by Yiagos and Prevost (1991) used an exponential function to assign V_s increasing with depth. On the other hand, Griffiths and Prevost (1988) assigned material properties to discrete layers of the dam, including a thin, shallow layer representing the rock shell. Our simulations using the elastic parameters adopted in these studies significantly overpredicted the peak seismic amplitudes on the dam, due to the presence of material with low seismic speed at the shallowest depth. A possible explanation for this

discrepancy is that V_s of the rock shell has increased over time due to variation of the water level (Clariá and Rinaldi, 2007; Dong and Lu, 2016) or internal deterioration. However, future work is needed to address this issue, such as via shallow seismic surveys on the dam.

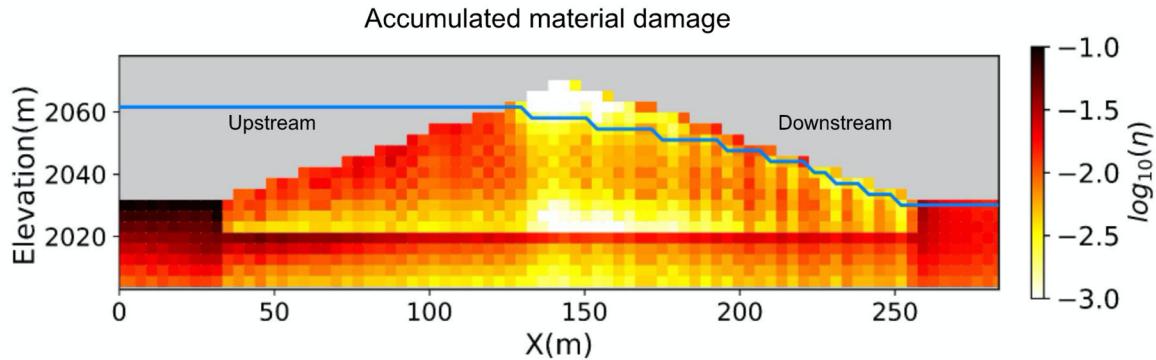


Figure 8. Accumulated material damage in the LVD from the HCF southward rupture scenario.

Based on the validations, we simulated both linear and nonlinear ground motions for a series of MCE rupture scenarios on the HCF, which is located within 8 km of the LVD. The southward rupture scenario generated the largest ground motions around the LVD, with PGAs exceeding 1 g considering the nonlinear rheology. However, plastic behavior in the LVD reduced PGVs and PGAs at the crest top by up to 2.5 times, with a highly complex wavefield. This reduction factor is similar to that found by Roten et al. (2014).

The effects on ground motions due to nonlinearity are expected to vary significantly with the nonlinear properties of the material, as shown by Roten et al. (2014, 2018). For this reason, we performed additional simulations with different cohesion values (c) and friction angles (ϕ) to estimate the variation of predicted ground motions due to uncertainties associated with the nonlinear properties of the LVD. Assuming that the cohesion used in our MCE simulation ($c=45$ kPa) is an upper bound for compacted clay, we considered two low-cohesion scenarios of $c=20$ kPa along with friction angles of 20° and 30° . The results of these simulations suggest another 30-40% reduction of horizontal PGAs when using lower cohesion, while the vertical motions appear mostly insensitive to the nonlinear parameters. Future studies should focus on acquiring more robust constraints on nonlinear properties of the studied structures. Finally, the simulations predict relatively small (~ 10 cm) settlements of the dam, with the largest displacements near the surface of the upstream side.

Acknowledgements

This research was supported by the California Geological Survey (Award #1020-006).

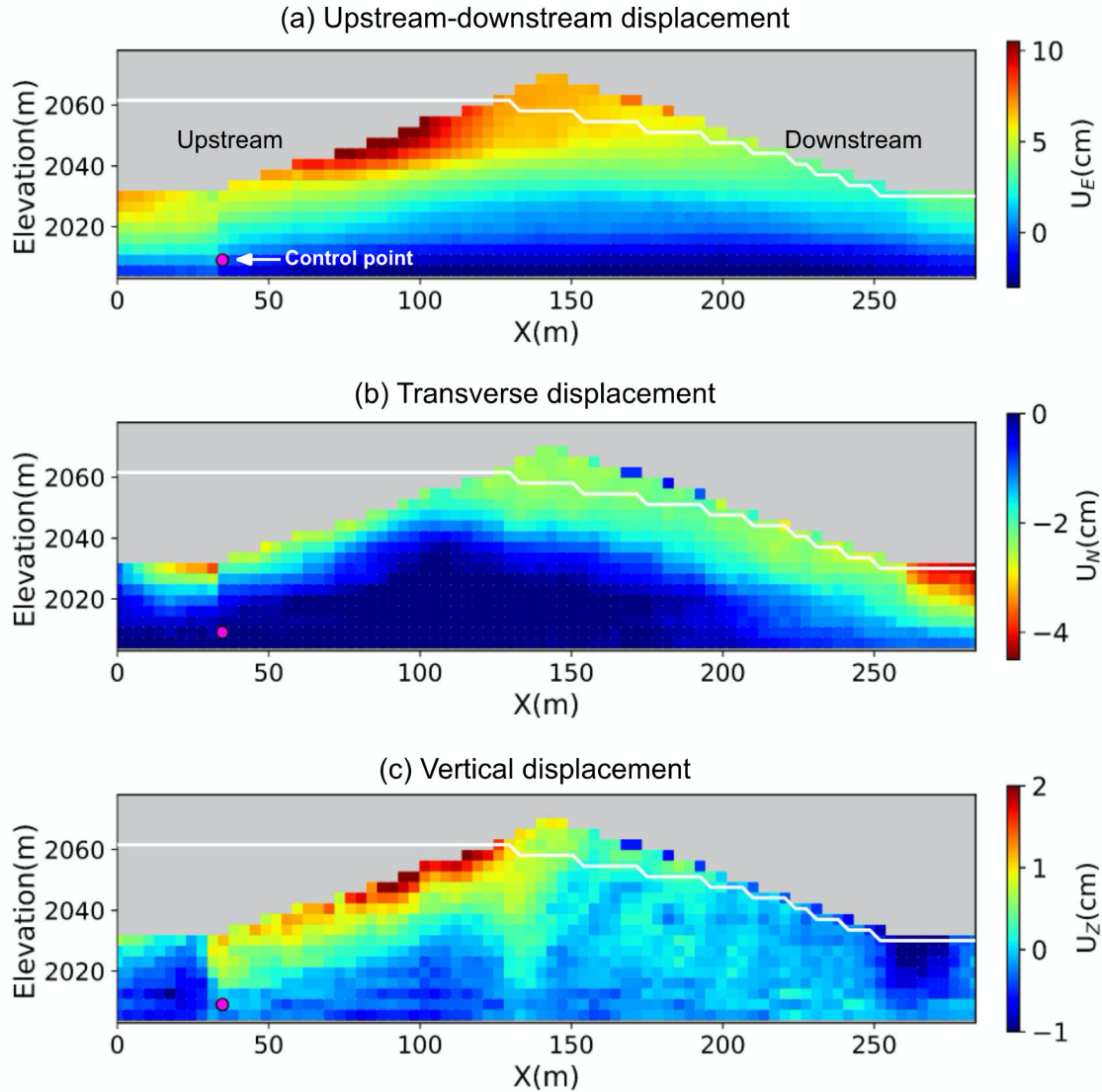


Figure 9. Relative displacement of the material within the LVD with respect to the control point (shown by the magenta dot) from the HCF southward rupture scenario.

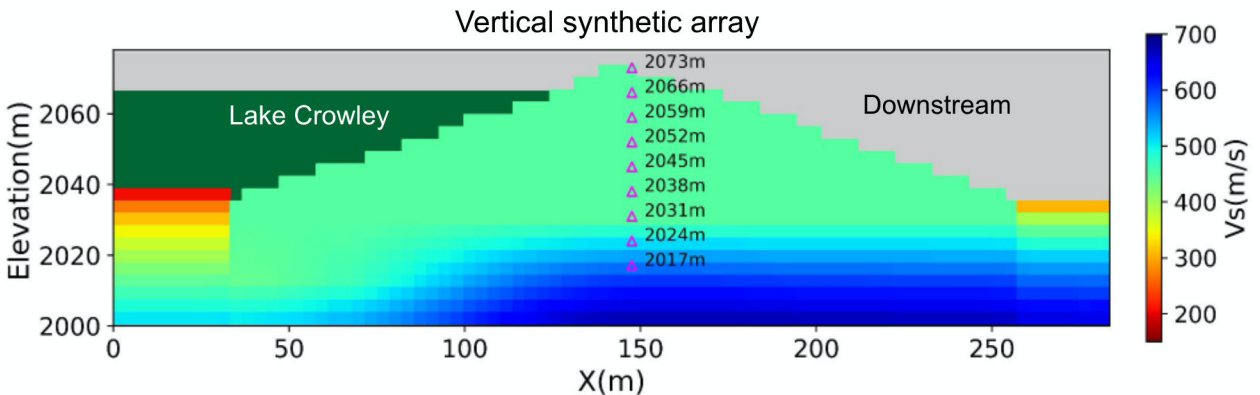


Figure 10. Locations of receivers in the virtual vertical array.

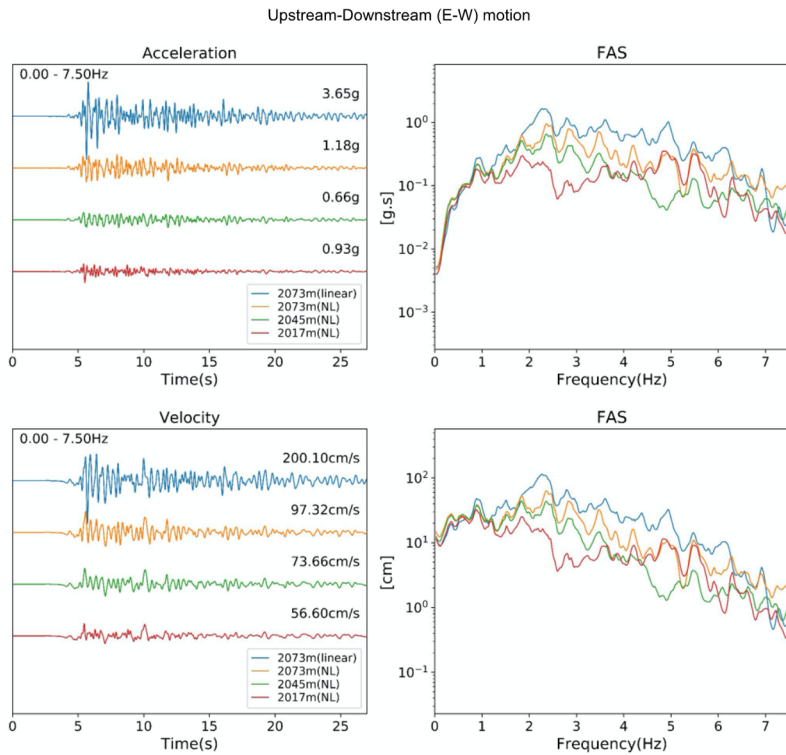


Figure 11. Comparison of nonlinear (top) acceleration and (bottom) velocity waveforms and FAS at stations at elevations of 2017 m (dam bottom), 2045 m, and 2073 m (dam crest surface), with the linear response at 2073 m for comparison (blue).

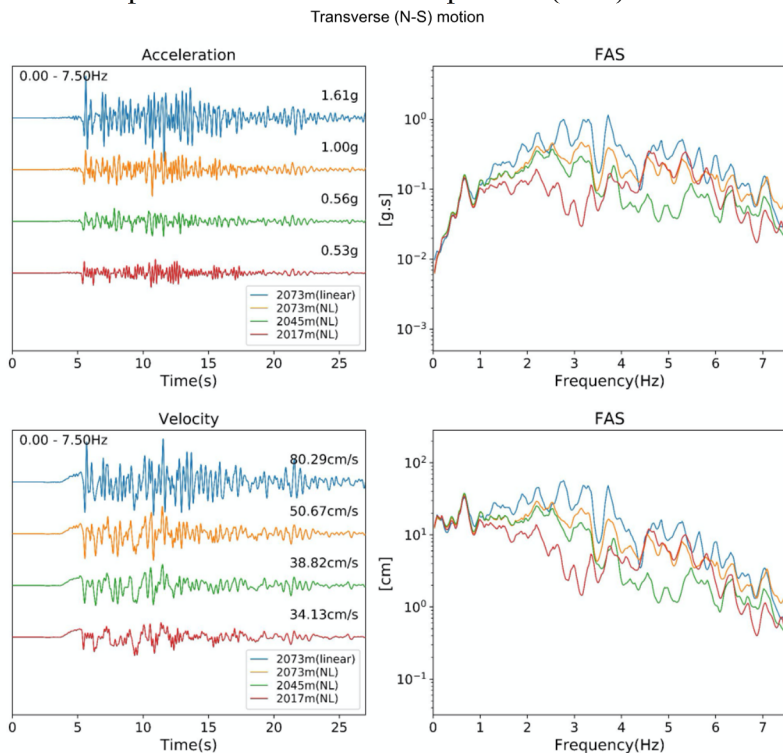


Figure 12. Same as Fig. 11, but for the transverse motion (N-S).

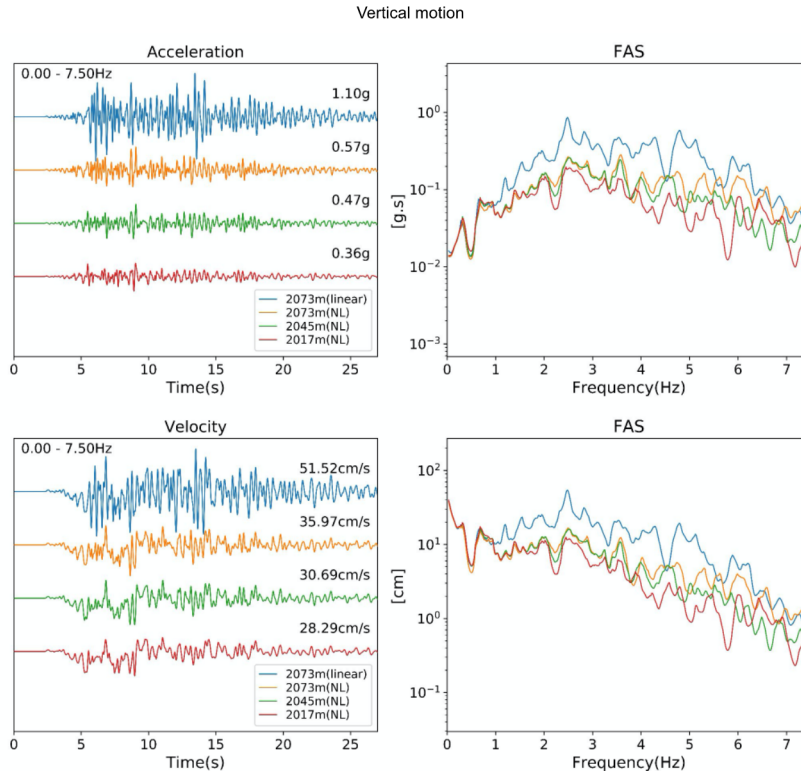


Figure 13. Same as Fig. 11, but for the vertical motion.

References

- Andrews, D. J. (2005). Rupture Dynamics with Energy Loss Outside the Slip Zone, *Journal of Geophysical Research: Solid Earth* 110.B1. ISSN: 2156-2202.
- Brune, J. N. (1970). Tectonic Stress and the Spectra of Seismic Shear Waves from Earthquakes, *Journal of Geophysical Research (1896-1977)* 75.26, pp. 4997–5009. ISSN: 0148-0227.
- Chen, R., Branum, D. M., Wills, C. J., & Hill, D. P. (2014). Scenario earthquake hazards for the Long Valley Caldera-Mono Lake area, east-central California (ver. 2.0, January 2018).
- Clariá, J. J. and Rinaldi, V. A. (2007). Shear Wave Velocity of a Compacted Clayey Silt, *Geotechnical Testing Journal* 30.5, pp. 399–408.
- Cockerham, R. S. and Corbett, E. J. (1987). The July 1986 Chalfant Valley, California, Earthquake Sequence: Preliminary Results, *Bulletin of the Seismological Society of America* 77.1, pp. 280–289. ISSN: 1943-3573.
- Cui, Y., Poyraz, E., Olsen, K. B., Zhou, J., Withers, K., Callaghan, S., Larkin, J., Guest, C., Choi, D, Chourasia, A., et al. (2013). Physics-based seismic hazard analysis on petascale heterogeneous supercomputers. Page 70 of: *Proceedings of SC13: International Conference for High Performance Computing, Networking, Storage and Analysis*. ACM.

- Dong, Y. and Lu, N. (2016). Dependencies of Shear Wave Velocity and Shear Modulus of Soil on Saturation, *Journal of Engineering Mechanics* 142.11, p. 04016083. ISSN: 1943-7889.
- Drucker, D. C. and Prager, W. (1952). *Soil Mechanics and Plastic Analysis or Limit Design*, *Quarterly of applied mathematics* 10.2, pp. 157–165.
- Ely, G. P., Jordan, T., Small, P., and Maechling, P. J. (2010). A V_s30 -derived near-surface seismic velocity model. AGU Fall Meet., San Francisco, California, 13–17 December, Abstract.
- FEMA, P. (2005). *Federal Guidelines for Dam Safety: Earthquake Analyses and Design of Dams*. FEMA 65.
- Graves, R. W. (1996). Simulating Seismic Wave Propagation in 3D Elastic Media Using Staggered-Grid Finite Differences, *Bulletin of the Seismological Society of America* 86.4, pp. 1091–1106. ISSN: 0037-1106.
- Graves, R., and Pitarka, A. (2016). Kinematic Ground-Motion Simulations on Rough Faults Including Effects of 3D Stochastic Velocity Perturbations, *Bulletin of the Seismological Society of America*, 106(5), 2136-2153. <https://doi.org/10.1785/0120160088>
- Griffiths, D. V., and Prevost, J. H. (1988). Two- and three-dimensional dynamic finite element analyses of the Long Valley Dam. *Géotechnique*, 38(3), 367-388. <https://www.icevirtuallibrary.com/doi/abs/10.1680/geot.1988.38.3.367>.
- Harris, R. A., Barall, M., Andrews, D. J., Duan, B., Ma, S., Dunham, E. M., Gabriel, A.-A., Kaneko, Y., Kase, Y., Aagaard, B. T., Oglesby, D. D., Ampuero, J.-P., Hanks, T. C., and Abrahamson, N. (2011). “Verifying a Computational Method for Predicting Extreme Ground Motion”. In: *Seismological Research Letters* 82.5, pp. 638–644. ISSN: 0895-0695.
- Hill, D. P. and Montgomery-Brown, E. (2015). Long Valley Caldera and the UCERF Depiction of Sierra Nevada Range-Front Faults. In: *Bulletin of the Seismological Society of America* 105.6, pp. 3189–3195. ISSN: 0037-1106.
- Hoek, E., Carranza-Torres, C., and Corkum, B. (2002). *Hoek-Brown Failure Criterion-2002 Edition*. Proceedings of NARMS-Tac 1.1, pp. 267–273.
- Hu, Z., K.B. Olsen, and S.M. Day (2022). Calibration of the Near-surface Seismic Structure in the SCEC Community Velocity Model Version 4, *Geophys. Jour. Int.*, 230, 2183-2198.
- Iwan, W. (1967). On a class of models for the yielding behavior of continuous and composite systems, *J. Appl. Mech*, 34(4):612–617.

- Lai, S.S., and Seed, H.B. (1985). Dynamic Response of Long Valley dam in the Mammoth Lake Earthquake Series of May 25–27 1980. Tech. rept. UCB/EERC-85/12. Earthquake Engineering Research Center.
- Leonard, M. (2010). Earthquake Fault Scaling: Self-Consistent Relating of Rupture Length, Width, Average Displacement, and Moment Release, *Bulletin of the Seismological Society of America* 100 (5A), pp. 1971–1988. ISSN: 0037-1106.
- Leonard, M. (2014). Self-Consistent Earthquake Fault-Scaling Relations: Update and Extension to Stable Continental Strike-Slip Faults, *Bulletin of the Seismological Society of America*, 104(6), 2953-2965. <https://doi.org/10.1785/0120140087>.
- Ma, S. (2008). A physical model for widespread near-surface and fault zone damage induced by earthquakes, *G3*, 9, 11, Q11009, doi:10.1029/2008GC002231 ISSN: 1525-2027.
- Nie, S., Wang, Y., Olsen, K. B., and Day, S. M. (2017). Fourth Order Staggered Grid Finite Difference Seismic Wavefield Estimation Using a Discontinuous Mesh Interface (WEDMI), *Bull. Seism. Soc. Am.* 107(5), 2183-2193.
- Olsen, K.B., Day, S.M., and C.R. Bradley (2003). Estimation of Q for long-period (>2 s) waves in the Los Angeles Basin, *Bull. Seis. Soc. Am.* 93, 627-638.
- O'Reilly, O., Yeh, T.-Y., Olsen, K.B., Hu, Z., Breuer, A., Roten, D., and Goulet, C. (2022). A high-order finite difference method on staggered curvilinear grids for seismic wave propagation applications with topography, *Bull. Seis. Soc. Am.*, 112 (1), 3-22, <https://doi.org/10.1785/0120210096>.
- Pacheco, J. and Nábelek, J. (1988). Source Mechanisms of Three Moderate California Earthquakes of July 1986, *Bulletin of the Seismological Society of America* 78.6, pp. 1907–1929. ISSN: 0037-1106.
- Roten, D., Olsen, K. B., Day, S. M., Cui, Y., and Fäh, D. (2014). Expected Seismic Shaking in Los Angeles Reduced by San Andreas Fault Zone Plasticity, *Geophysical Research Letters* 41.8, pp. 2769–2777. eprint: <https://agupubs.onlinelibrary.wiley.com/doi/pdf/10.1002/2014GL059411>.
- Roten, D., Cui, Y., Olsen, K. B., Day, S. M., Withers, K., Savran, W. H., Wang, P., and Mu, D. (2016). High-Frequency Nonlinear Earthquake Simulations on Petascale Heterogeneous Supercomputers, *SC '16: Proceedings of the International Conference for High Performance Computing, Networking, Storage and Analysis*, pp. 957–968.
- Roten, D., Olsen, K. B., Day, S. M., and Cui, Y. (2018). Quantification of Fault-Zone Plasticity Effects with Spontaneous Rupture Simulations, *Best Practices in Physics-based Fault Rupture Models for Seismic Hazard Assessment of Nuclear Installations*. Ed. by L. A. Dalguer, Y. Fukushima, K. Irikura, and C. Wu. Cham: Springer International Publishing, pp. 45–67. ISBN: 978-3-319-72709-7.

- Savage, J. C. and Gross, W. K. (1995). Revised Dislocation Model of the 1986 Chalfant Valley Earthquake, Eastern California, *Bulletin of the Seismological Society of America* 85.2, pp. 629–631. ISSN: 0037-1106.
- Savitzky, A. and Golay, M. J. (1964). Smoothing and Differentiation of Data by Simplified Least Squares Procedures, *Analytical chemistry* 36.8, pp. 1627–1639.
- Seed, H. B., Makdisi, F. I., and Alba, P. D. (1978). Performance of Earth Dams During Earthquakes, *Journal of the Geotechnical Engineering Division* 104.7, pp. 967–994.
- Small, P., Gill, D., Maechling, P. J., Taborda, R., Callaghan, S., Jordan, T. H., et al. (2017). The SCEC Unified Community Velocity Model Software Framework, *Seismological Research Letters*, 88(6), 1539-1552. <https://doi.org/10.1785/0220170082>
- Smith, K. D., and Priestley, K. F. (2000). Faulting in the 1986 Chalfant, California, Sequence: Local Tectonics and Earthquake Source Parameters, *Bulletin of the Seismological Society of America*, 90(4), 813-831. <https://doi.org/10.1785/0119990129>
- Townsend, K. F., Clark, M. K., and Zekkos, D. (2021). Profiles of Near-Surface Rock Mass Strength Across Gradients in Burial, Erosion, and Time, *Journal of Geophysical Research: Earth Surface* 126.4, e2020JF005694. ISSN: 2169-9003.
- Wills, C. J., Gutierrez, C. I., Perez, F. G., and Branum, D. M. (2015). A Next Generation Vs30 Map for California Based on Geology and Topography. *Bulletin of the Seismological Society of America*, 105(6), 3083-3091. <https://doi.org/10.1785/0120150105>
- Withers, K. B., Olsen, K. B., and Day, S. M. (2015). Memory-Efficient Simulation of Frequency-Dependent Q Memory-Efficient Simulation of Frequency-Dependent Q, *Bulletin of the Seismological Society of America* 105.6, pp. 3129–3142. ISSN: 0037-1106.
- Yiagos, A. N. and Prevost, J. H. (1991). Two-Phase Elasto-Plastic Seismic Response of Earth Dams: Applications, *Soil Dynamics and Earthquake Engineering* 10.7, pp. 371–381. ISSN: 0267-7261.
- Zeghal, M. and Abdel-Ghaffar, A. M. (1992). Analysis of Behavior of Earth Dam Using Strong motion Earthquake Records, *Journal of Geotechnical Engineering* 118.2, pp. 266–277.